



Nanostructured ceria-praseodymia catalysts for diesel soot combustion



Tahrizi Andana, Marco Piumetti, Samir Bensaid*, Nunzio Russo, Debora Fino, Raffaele Pirone

Department of Applied Science and Technology, Politecnico di Torino, Corso Duca degli Abruzzi 24, 10129 Turin, Italy

ARTICLE INFO

Article history:

Received 5 August 2015

Received in revised form

14 December 2015

Accepted 15 December 2015

Available online 21 December 2015

Keywords:

Ceria

Ceria-praseodymia

Soot oxidation

Nanocubes

Nanorods

ABSTRACT

Nanostructured ceria-praseodymia catalysts with different praseodymium contents have been prepared through hydrothermal synthesis to study the effect of Pr as a dopant and the effect of morphology towards soot combustion under “loose” and “tight” soot-catalyst conditions. Samples synthesized through solution combustion synthesis (SCS) have also been prepared as comparative materials. Studies in physicochemical properties of the catalysts have been carried out using complementary techniques. The present work also resorts to soot-TPR as an unconventional method of investigating the ability of solid catalysts to initiate soot oxidation in the absence of bulk oxygen. Ce50Pr50 catalyst (where 50 indicates the atomic percentage of cerium as well as of praseodymium) with mixed structures of nanorods and nanocubes has attained the best catalytic performances, thanks to the high lattice oxygen mobility and the easy reducibility. The insertion of Pr cations to the ceria framework enhances the number of redox sites on the surface, thus generating more oxygen vacancies. As a whole, activity tests in general have proven that despite having relatively low surface areas, ceria-praseodymia nanocubes and nanorods facilitated soot combustion reaction more actively than SCS-based ceria-praseodymia catalysts with larger surface areas. This evidences the beneficial effect of well-defined nanostructures in soot combustion, due to their possession of highly reactive low-index facets (1 0 0) and (1 1 0). Within SCS-based samples, however, the specific surface area overshadows the importance of praseodymium. This eventually marks the synergistic combination of well-defined nanostructures and praseodymium as a dopant.

© 2015 Elsevier B.V. All rights reserved.

1. Introduction

Diesel engines have long been used to power heavy duty vehicles and long haul trucks for distant travels. Having better combustion and fuel economy than gasoline engines, the use of diesel engines has successfully reached the market of passenger cars. However, this expansion entails the alarming rise of air pollutants, among which diesel soot is of particular concern due to its negative impact on cardiovascular health. In response to the rigorous emission standards issued in Euro VI, continuous endeavors have been exerted in improving the abatement of diesel soot. In the presence of oxygen, soot burns naturally at above 600 °C; however, diesel exhaust gas temperature falls in the range of 200–500 °C [1]. Oxidation catalysts are known to provide active oxygen species that promptly

reacts with soot. Therefore, the use of oxidation catalysts enables soot combustion at low temperature.

Ceria emerges among the most investigated catalysts for soot oxidation following its successful use in three-way catalytic converters (TWC) [2–4]. The redox behavior bestowed on ceria allows it to release and consume oxygen under reduction and oxidation cycles. This behavior results in alternating oxygen composition between CeO_2 and CeO_{2-x} (Ce^{4+} and Ce^{3+}) [5], the latter refers to the substoichiometric ceria with oxygen vacancies. The insertion of metallic dopants into the lattice of ceria creates structural defects and consequently enhances the catalytic properties, such as oxygen storage capacities (OSC) and oxygen mobility [6,7]. Praseodymium, in particular, has recently received much attention due to its beneficial effect on ceria [8,9]. Akin to ceria, praseodymium oxide (Pr_6O_{11}) has equally a fluorite structure with similar crystal dimensions. The aliovalency of praseodymia (Pr^{3+} and Pr^{4+}) exists in its pure oxide and even in its solid solution with ceria. Therefore, ceria-praseodymia mixed oxides promote higher mobility of oxygen ions

* Corresponding author.

E-mail address: samir.bensaid@polito.it (S. Bensaid).

and currently have the best performance in soot combustion among other ceria-based catalysts [6,10–13].

Despite the ability to provide active oxygen to the reaction, oxidation catalysts for low temperature soot combustion require additionally effective interactions between soot and catalyst surfaces [14,15]. Highly reactive surfaces can be attained by tailoring the morphology of the catalysts. The potential of nanostructured materials as active catalysts has long been investigated thanks to their high surface-to-volume ratio and their quantum size effects [16,17]. Nanomaterials are present in a vast spectrum of shapes composed of various exposed planes. Each plane possesses a specific surface energy which characterizes the stability of the surface towards a reaction. Low surface energy induces low surface instability and enhances the reactivity of the corresponding plane [18].

Nanostructured ceria emerges as a versatile material that can be engineered into various shapes like nanorod and nanocube [19–22]; each structure is present with its respective constituting planes. Ceria nanoparticles with abundant (110) and (100) planes gives higher OSC than those with (111) planes [22,23]. This suggests the high catalytic activity in ceria nanorods and nanocubes towards oxidation reaction compared to the one in ceria nanopolyhedra. In addition, exposure of (100) planes in ceria nanocubes results in remarkable oxidation activity of soot [20] and CO [22]. However, to the best of author's knowledge, studies in morphology and surface reactivity of nanostructured ceria-praseodymia have never been reported in the literature. Combining high oxygen mobility promoted by praseodymium and high surface reactivity as the outcome of proper morphology is thus expected to maximize soot combustion activity.

This work investigates the activity of a series of new nanostructured ceria-praseodymia in soot oxidation under different reaction conditions ("loose" and "tight" soot-catalyst contacts). A set of ceria-praseodymia catalysts synthesized through solution combustion synthesis (SCS) was also prepared for comparison. This work is accompanied with studies in physicochemical properties of the synthesized catalysts using complementary techniques.

2. Experimental

2.1. Preparation of the catalysts

Nanostructured ceria-praseodymia catalysts were synthesized through hydrothermal process using nitrates of cerium and praseodymium as the precursors. Catalysts with four molar compositions Ce(%)–Pr(%) = Ce(100)–Pr(0), Ce(90)–Pr(10), Ce(75)–Pr(25) and Ce(50)–Pr(50) were prepared and further denoted as Ce100, Ce90Pr10, Ce75Pr25 and Ce50Pr50 respectively. A typical preparation of Ce50Pr50 involved dissolving initially 5 mmol of Ce(NO₃)₃·6H₂O (Sigma–Aldrich) and 5 mmol of Pr(NO₃)₃·6H₂O (Sigma–Aldrich) in 10 mL deionized water. 1.2 mol of NaOH pellets (Sigma–Aldrich) were initially dissolved in 70 mL deionized water and stirred. The solution of salt precursors was then added dropwise into the continuously stirring NaOH solution, followed by the formation of pale green slurry. The mixture was then left for additional stirring for 1 h. The final slurry was transferred to an autoclave (200 mL) in which deionized water was added to reach minimum 75% of the total autoclave volume. The slurry was then aged at 180 °C for 24 h. The fresh precipitates were then separated by centrifugation, washed with ethanol and deionized water several times, and dried at 60 °C overnight. Finally, the dry solids were ground and calcined at 550 °C for 4 h.

Comparative samples of ceria-praseodymia were synthesized through solution combustion synthesis. For the preparation of the sample Ce50Pr50–SCS, 1.9 g of Ce(NO₃)₃·6H₂O and 1.9 g of Pr(NO₃)₃·6H₂O were mixed in 60 mL deionized water along with

1.6 g of urea. The resulting solution was transferred into a ceramic crucible and placed in a furnace at 650 °C for 20 min.

2.2. Characterization of the catalysts

Powder X-ray diffraction patterns were recorded on an X'Pert Philips PW3040 diffractometer using Cu K α radiation. The intensity data were collected over a 2 θ range of 20–70° with a 0.013° step size and using a counting time of 0.2 s per step. The diffraction peaks were identified using powder diffraction files by International Centre of Diffraction Data (ICDD). From these identified peaks, the lattice parameters, a_0 , of the samples were subsequently calculated through Rietveld refinement. Particle size was estimated by applying Scherrer's equation, $D = 0.9\lambda/b\cos\theta$, where λ is the wavelength of the Cu K α radiation, b is full width at half maximum (FWHM) in radians, 0.9 is the shape factor for spherical particles and θ is the angle of diffraction peaks.

The BET specific surface area (S_{BET}) and total pore volume (V_p) were determined by N₂ physisorption at –196 °C on a Micrometrics ASAP 2020 instrument. Prior to the analyses, the samples were degassed at 200 °C for 2 h to remove water and other atmospheric contaminants. The specific surface area of the samples was calculated using the BET method.

Sample morphology was observed through a field emission scanning electron microscope (FESEM Zeiss MERLIN, Gemini-II column). The Ce and Pr contents in all samples were determined through EDX analysis (Oxford X-ACT).

XPS (X-ray photoelectron spectroscopy) measurements were obtained on XPS PHI 5000 Versa probe apparatus using band-pass energy of 187.85 eV, a 45° take off angle and a 100.0 μ m diameter X-ray spot size. Curve-fits were performed by means of Multipack 9.0 software.

Reducibility of catalysts was investigated through CO-TPR and soot-TPR. CO-TPR analysis was carried out in a fixed bed micro reactor (a quartz U-tube, with an inner diameter of 4 mm, heated by an electric, PID-regulated furnace). A reactor bed containing 150 mg of silica and 45 mg of catalysts was placed in a quartz tube, then put in contact with reducing flowing gas (2000 ppm CO in N₂, 200 mL min^{–1}) and heated from ambient temperature to 750 °C with heating rate at 10 °C min^{–1}). CO consumption and CO₂ production were continuously recorded in NDIR analyzers (ABB Uras 14). Before analysis, sample was pretreated with synthetic air for 2 h followed by flushing with N₂ for 30 min. Soot-TPR was additionally conducted to investigate catalyst reduction and active oxygen phenomena in the presence of soot. A bed mixture containing 5 mg of carbon soot (Printex-U), 45 mg of catalyst and 150 mg of silica was prepared in "tight contact" (more details in Section 2.3) and put inside the fixed-bed micro-reactor. An inert gas comprising pure nitrogen was fed to the reactor at a rate of 100 mL min^{–1}. The temperature of the furnace was programmed to increase from ambient to 750 °C by 5 °C per minute. CO and CO₂ concentrations in the reactor outlet were similarly measured in the NDIR analyzers.

2.3. Catalytic activity tests

A classical temperature programmed combustion (TPC) was applied to carry out catalytic tests for soot oxidation. Tests were carried out in a fixed-bed micro-reactor (a quartz U-tube, with an inner diameter of 4 mm, heated by an electric, PID-regulated furnace). A thermocouple was placed as close as possible to the catalytic bed, still not being in direct contact. An oxidizing atmosphere containing 50%-vol of air and 50%-vol of N₂ was fed at a constant rate of 100 mL min^{–1} to the reactor. The catalytic bed was prepared by mixing 5 mg of carbon soot, 45 mg of powdered catalyst, and 150 mg of inert silica. The bed mixture was prepared in two ways to simulate their respective soot-catalyst conditions, namely

Table 1Textural properties of the samples derived from N_2 physisorption at 77 K and X-ray diffraction.

Catalyst	S_{BET} ($m^2 g^{-1}$)	V_p ($cm^3 g^{-1}$)	Particle size (nm) ^a	Lattice parameter, a_0 (nm) ^b
Ce50Pr50	20	0.05	43	0.5419
Ce75Pr25	12	0.03	58	0.5414
Ce90Pr10	9	0.03	80	0.5414
Ce100	6	0.02	71	0.5411
Ce50Pr50-SCS	14	0.05	21	0.5427
Ce75Pr25-SCS	16	0.03	27	0.5426
Ce90Pr10-SCS	33	0.04	35	0.5419
Ce100-SCS	43	0.04	32	0.5411

^a Obtained by applying Scherrer's equation.^b Obtained from Rietveld refinement.

“loose” and “tight”. The former was achieved by gently stirring the bed mixture with a spatula for 2 min. Homogeneous mixture was attainable and both solid phases were still kept loosely in contact. The latter, on the other hand, was obtained by ball-milling the bed mixture at 250 rpm for 10 min to eventually attain intimate soot-catalyst contact. This contact allows a proper discrimination of the activity of different catalysts despite being unrepresentative of the real soot-catalyst contact in a diesel particulate filter (DPF).

The reaction temperature was programmed to increase from 100 to 700 °C with 5 °C min⁻¹ heating rate. CO and CO₂ concentrations in the reactor outlet were measured in NDIR analyzers (ABB Uras 14). The temperatures corresponding to 10%, 50% and 90% soot conversion (denoted as $T_{10\%}$, $T_{50\%}$, $T_{90\%}$, respectively) were taken as indices of the catalytic activity.

3. Result and discussion

3.1. Textural and redox properties of the samples

Table 1 shows the primary textural properties of all samples, obtained from X-ray diffractogram and isotherms of N_2 physisorption at 77 K.

Fig. 1 shows the powder XRD patterns of the nanostructured catalysts (**Fig. 1a**) and SCS-based catalysts (**Fig. 1b**). All catalysts refer to a typical cubic fluorite structure marked by the appearance of (111), (200), (220), (311), (222) and (400) planes [24]. The lattice parameters of praseodymium-doped ceria samples are higher than those of pure ceria samples. This is due to the similar ionic radius of Ce⁴⁺/Ce³⁺ and Pr⁴⁺/Pr³⁺ (0.97/1.14 Å and 0.96/1.13 Å, respectively) [25]. The lattice expansion in some samples might be ascribed to the presence of more Pr³⁺ cations, since Pr⁴⁺ is more reducible than Ce⁴⁺ [10].

On the other hand, it could be possible that some Pr species are located into interstitial sites.

Scherrer's equation predicts that samples with higher praseodymium contents exhibit lower crystallite sizes, likely due to different hydrolysis and condensation kinetics during the synthesis procedure. This finding was observed for both morphologies of catalysts: nanostructured particles and SCS powders. SCS-based catalysts are, nevertheless, estimated to have the lowest crystallite sizes.

Low BET surface areas are generally obtained in nanostructured ceria-based catalysts; the lowest one is obtained in pure nanostructured ceria, Ce100 ($S_{BET} = 6 m^2 g^{-1}$ and $V_p = 0.02 cm^3 g^{-1}$). In the case of nanostructured catalysts, the addition of praseodymium appears to increase the surface area of the catalysts. This suggests the possibility of praseodymium in modifying the ripening process, leading to smaller final size of the nanoparticles. On the other hand, in the case of SCS-based catalysts, the addition of praseodymium lowers the surface area. Krishna et al. [8,26] encountered equally the phenomena of the decreasing surface area

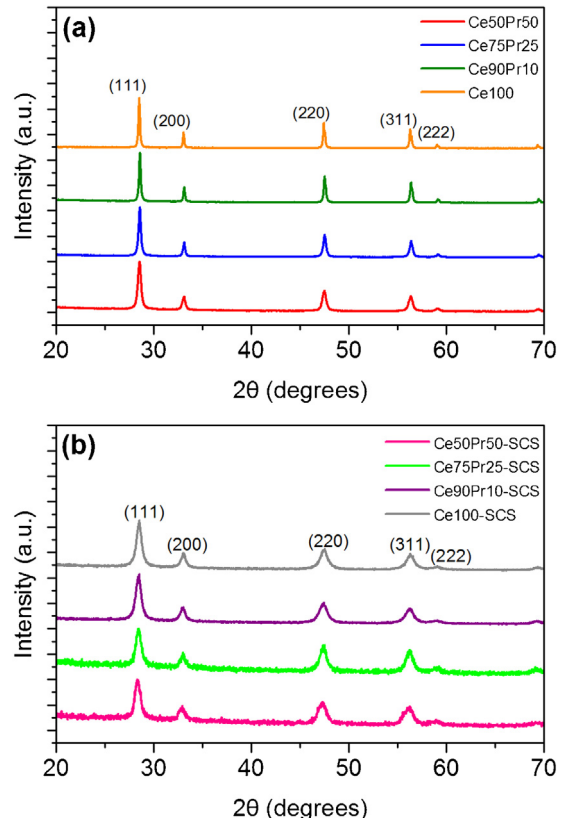


Fig. 1. Powder X-ray diffractogram of all samples: (a) nanostructured catalysts and (b) SCS-based catalysts.

in ceria-praseodymia samples; the surface area was even the lowest for pure praseodymium oxide.

FE-SEM analysis has been conducted to investigate the morphology of the samples, confirming the textural properties obtained previously by N_2 physisorption. **Fig. 2** reports the FE-SEM images of all nanostructured samples. Ce100 sample (**Fig. 2a**) has the morphology of nanocubes, comprising six well-defined (100) surfaces. The size of the nanocubes varies from 100 to 300 nm. Nanocubes are still observed in Ce90Pr10 sample (**Fig. 2b**) but their size is rather smaller than those in Ce100 (50–200 nm). This sample noticeably features nanorods, which originate most likely from the elongation of nanocubes. This suggests the effect of praseodymium on changing crystal orientation. The same phenomena are also encountered in Ce75Pr25 sample (**Fig. 2c**), having more abundant nanocubes with small dimension than those in Ce90Pr10 sample. Ce50Pr50 sample (**Fig. 2d**), having the highest praseodymium content, possesses a clear distinction between nanocubes and nanorods. The size of nanocubes is mostly lower than 50 nm. Nanorods seem

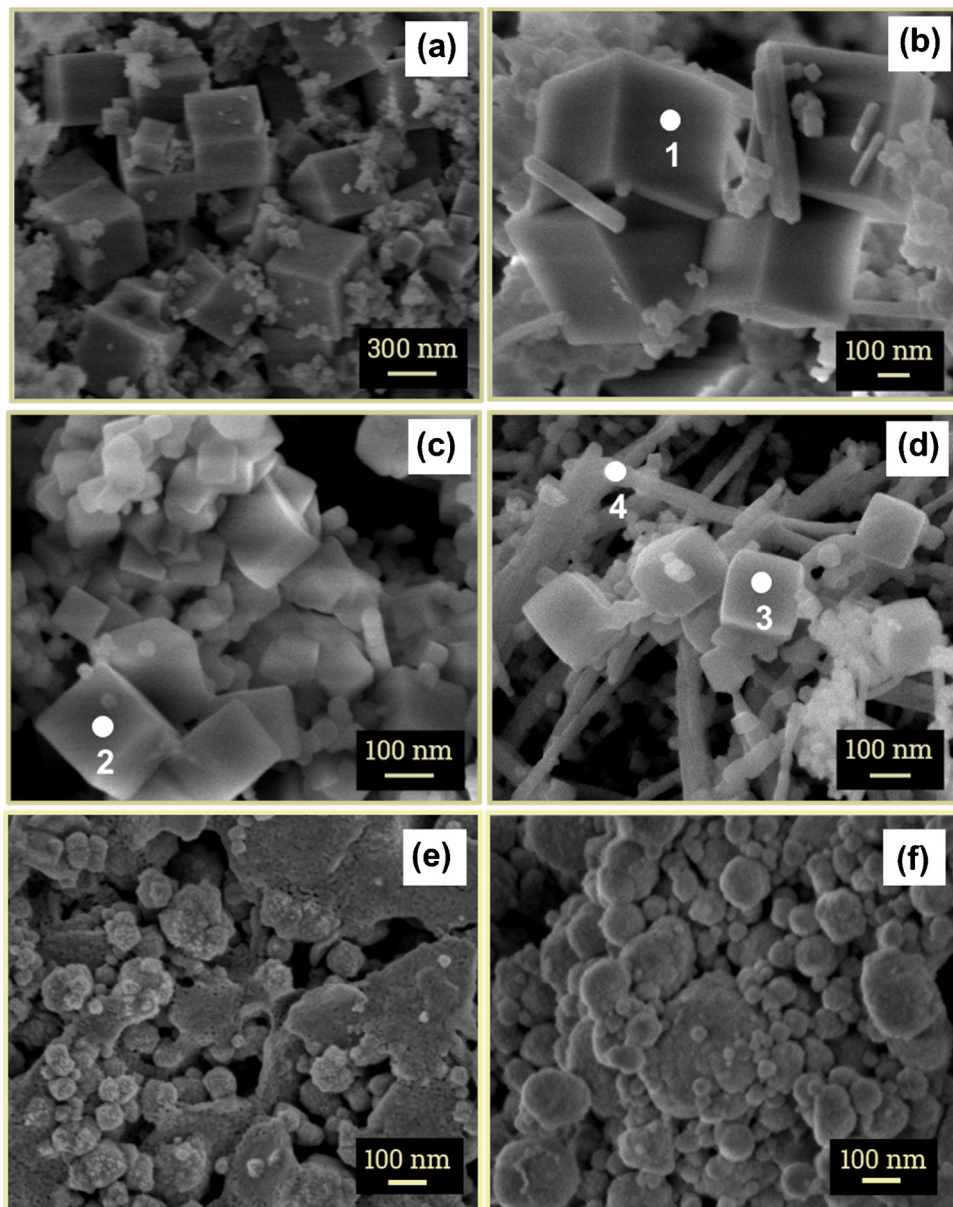


Fig. 2. FE-SEM images of the nanostructured catalysts: (a) Ce100, (b) Ce90Pr10, (c) Ce75Pr25, (d) Ce50Pr50, (e) Ce50Pr50-SCS and (f) Ce90Pr10-SCS.

to dominate in this sample, suggesting that the crystal orientation starts to be fully controlled by praseodymium. Previous research have reported that synthesizing praseodymium oxide (Pr_6O_{11}) in nanoscale results mostly in nanorods [27–29]. On the other hand, materials prepared via SCS (i.e., Ce50Pr50-SCS and Ce90Pr10-SCS, corresponding to Fig. 2e and f, respectively) exhibit spongy structures (three-dimensional framework solids) formed by agglomerates of small particles. Their porous structure is due to the fact that during the SCS procedure the reacting precursors release a large amount of gaseous products in a short period of time, thus leading to foamy catalyst morphology.

Energy dispersive X-ray analysis (EDS) was also carried out to confirm the atomic percentage between Ce, Pr and O atoms in the samples. Table 2 summarizes the composition of the samples derived from EDS analysis on a certain area shown in Fig. 2 (indicated by points and numbers). In all mixed oxide samples, the cerium-to-praseodymium atomic ratios are in a good agreement with their theoretical values. This ratio is even similar for both nanocubes and nanorods that coexist in the Ce50Pr50 sample.

Table 2

Atomic percentages of Ce, Pr and O in the mixed oxide samples derived from Energy dispersive X-ray analysis (EDS).

Catalyst	Atomic percentage from EDX			Theoretical atomic percentage		
	Ce	Pr	O	Ce	Pr	O
Ce50Pr50 (point 3)	13	11	76	17	17	66
(point 4)	36	33	31			
Ce75Pr25 (point 2)	23	9	68	25	8.3	66
Ce90Pr10 (point 1)	37	5	58	30	3.3	66
Ce50Pr50-SCS	14	19	67	17	17	66
Ce75Pr25-SCS	23	8	69	25	8.3	66
Ce90Pr10-SCS	31	4	65	30	3.3	66

Fig. 3 reports the XPS spectra of all samples in the O 1s core level. Two distinctive peaks were assigned in the spectra to chemisorbed oxygen ($\text{O}\alpha$) and lattice oxygen ($\text{O}\beta$) respectively. The peaks in lower binding energy (527.8–528.8 eV) were ascribed to $\text{O}\beta$ (i.e., O^{2-}) while those in higher binding energy (530.1–531.4 eV) corre-

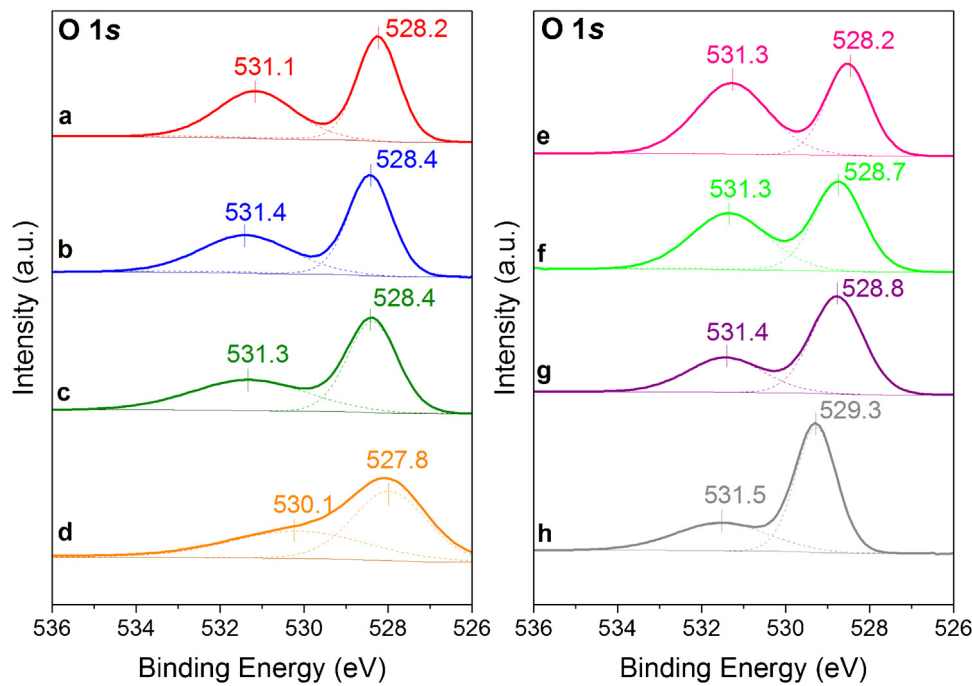


Fig. 3. XPS spectra of the (a) Ce50Pr50, (b) Ce75Pr25, (c) Ce90Pr10, (d) Ce100, (e) Ce50Pr50-SCS, (f) Ce75Pr25-SCS, (g) Ce90Pr10-SCS and (h) Ce100-SCS in the O 1s core level region.

spond to O α (i.e., O $_2^{2-}$, O $^-$, OH $^-$, CO $_3^{2-}$) [20,30–33]. Samples with high praseodymium contents, irrespective of morphology, exhibit richer oxygen at the surface than in the oxide framework; the atomic percentages of the oxygen species can be seen in Table 3. High amount of α -species fosters oxygen spillover at the oxide surface and this may have a beneficial effect on the oxidation activity [34]. As a whole, in oxidation catalysis spillover oxygen may act as: (i) the controller of active sites and (ii) the reactant. This means that when catalytic sites are rich in spillover oxygen (the so-called “active oxygen”), the surface of the catalyst becomes very efficient in facilitating soot combustion reaction.

Table 3
Results of curve-fittings on O 1s binding energies of catalysts.

Sample	O α		O β	
	(% atom)	BE (eV)	(% atom)	BE (eV)
Ce50Pr50	45.5	531.1	54.5	528.2
Ce75Pr25	44.6	531.4	55.4	528.4
Ce90Pr10	44.0	531.3	56.0	528.4
Ce100	41.9	530.1	58.1	527.8
Ce50Pr50-SCS	56.5	531.3	43.5	528.5
Ce75Pr25-SCS	49.8	531.3	50.2	528.7
Ce90Pr10-SCS	34.5	531.4	65.5	528.8
Ce100-SCS	33.6	531.5	66.4	529.3

Table 4A
Results of curve-fittings on Ce 3d binding energies of catalysts.

Ce 3d $_{5/2}$								
Sample	v $_0$ (Ce $^{4+}$)		v $_1$ (Ce $^{3+}$)		v $_2$ (Ce $^{4+}$)		v $_3$ (Ce $^{4+}$)	
	(% atom)	BE (eV)						
Ce50Pr50	13.7	881.3	11.9	882.7	17.4	887.9	24.0	897.3
Ce75Pr25	13.2	881.5	13.0	882.8	17.6	888.2	23.2	897.5
Ce90Pr10	15.7	881.6	10.3	883.2	17.2	888.1	22.9	897.5
Ce100	17.3	881.0	12.7	883.0	14.0	887.5	15.2	896.7
Ce50Pr50-SCS	11.6	881.7	11.3	882.9	14.1	888.0	23.3	897.7
Ce75Pr25-SCS	14.6	881.9	12.2	883.5	16.0	888.3	21.2	898.0
Ce90Pr10-SCS	14.1	881.9	14.5	883.2	17.8	888.3	22.8	897.8
Ce100-SCS	21.9	882.3	8.67	884.9	15.4	888.6	20.2	898.3

Ce 3d $_{3/2}$								
Sample	u $_0$ (Ce $^{4+}$)		u $_1$ (Ce $^{3+}$)		u $_2$ (Ce $^{4+}$)		u $_3$ (Ce $^{4+}$)	
	(% atom)	BE (eV)						
Ce50Pr50	7.20	899.8	3.87	900.7	5.72	906.7	16.3	915.7
Ce75Pr25	5.66	900	5.61	900.7	5.25	906.9	16.5	915.9
Ce90Pr10	7.63	900	4.03	901.1	6.22	906.9	16.1	915.9
Ce100	20.1	899.3	0.42	903.1	5.51	906.3	14.8	915.4
Ce50Pr50-SCS	6.25	900.2	5.3	901.2	9.37	907.5	18.8	916.2
Ce75Pr25-SCS	7.13	900.4	4.93	901.5	7.56	907.4	16.3	916.3
Ce90Pr10-SCS	6.3	900.4	4.02	901.3	4.64	907.2	15.9	916.3
Ce100-SCS	8.01	900.9	6.98	902.5	5.53	907.4	13.4	916.7

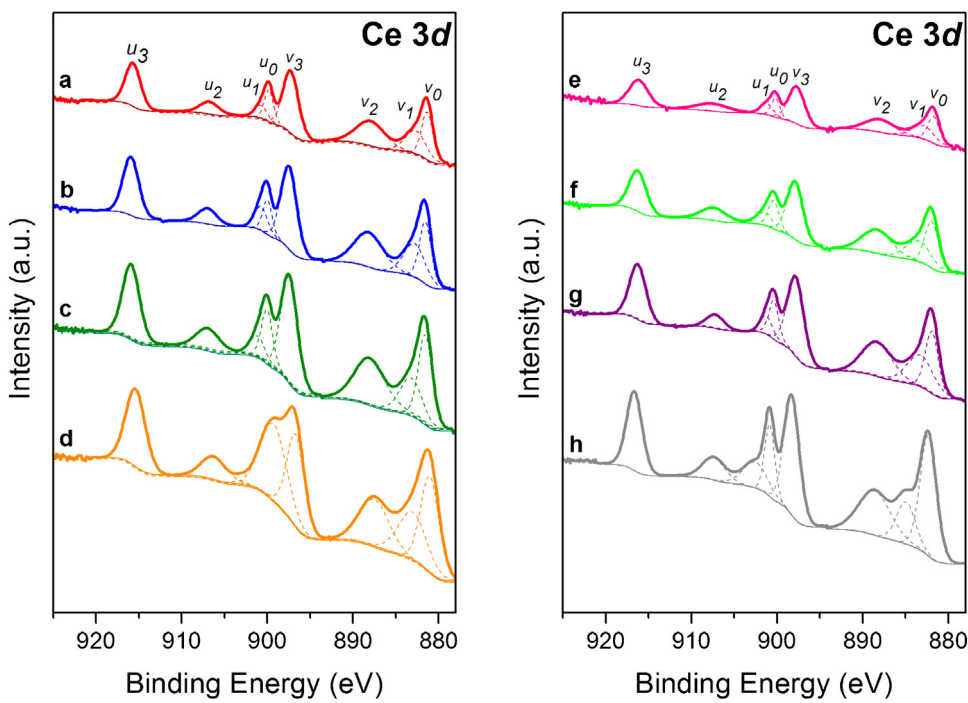


Fig. 4. XPS spectra of the (a) Ce50Pr50, (b) Ce75Pr25, (c) Ce90Pr10, (d) Ce100, (e) Ce50Pr50-SCS, (f) Ce75Pr25-SCS, (g) Ce90Pr10-SCS samples and (h) Ce100-SCS in the Ce 3d core level region.

Table 4B
Concentrations of Ce³⁺ (%) estimated by XPS signals on Ce 3d binding energies.

Sample	Ce ³⁺ ($v_1 + u_1$) (%)
Ce50Pr50	15.8
Ce75Pr25	18.6
Ce90Pr10	14.3
Ce100	13.2
Ce50Pr50-SCS	16.6
Ce75Pr25-SCS	17.2
Ce90Pr10-SCS	18.5
Ce100-SCS	15.7

Fig. 4 shows the Ce 3d core-level spectra of all samples, in which “u” and “v” peaks correlate with $3d_{5/2}$ and $3d_{3/2}$ states, respectively. The doublets (v_0, u_0), (v_2, u_2), and (v_3, u_3) were attributed to the Ce⁴⁺ state while the doublet (v_1, u_1) was ascribed to the Ce³⁺ state [35]. **Tables 4A and B** summarize the relative abundances of Ce³⁺ and Ce⁴⁺ (in atomic percentage, %) estimated from deconvoluted peaks of the Ce 3d spectra. The analysis suggests that cerium is present at the surface in both 3+ and 4+ oxidation states and the primary valence of cerium in mixed Ce–Pr oxides is 4+. The incorporation of praseodymium, regardless of the synthesis, enhances the redox sites of Ce³⁺ at the surface (see **Table 4B**). Higher Ce³⁺ concentrations at the surface were encountered in SCS-based samples, due to the high temperature (600 °C) and the exothermicity of the SCS reaction.

Fig. 5 shows finally the Pr 3d core-level XPS spectra of all samples containing praseodymium (excluding pure ceria). The peaks in the spectra were identified in two different states: (i) Pr 3d_{5/2} at lower binding energies (927–933 eV), in which two peaks, *m* and *s*, were designated, and (ii) Pr 3d_{3/2} at higher binding energies (952–965 eV), in which four peaks, *m'*, *s'*, *t'* and *f* were assigned. The denotation *m,m'* and *s,s'* refers to “main” and “satellite” peaks respectively while *t'* refers to extra structure existing only in 3d_{3/2} component [36]. All spectra show close resemblance to the Pr₂O₃ spectra reported elsewhere [37,38]. However, the spectra of samples with high praseodymium contents possess additional peak

f at BE of 965 eV, referring to the $3d4f^1$ final state, which is not observed in the spectra of pure Pr and Pr₂O₃ [37]. Therefore this peak uniquely originates from PrO₂ and marks the existence of Pr⁴⁺ oxidation state [36,37,39]. This means that in the ceria framework, both Pr³⁺ and Pr⁴⁺ oxidation states exist. However, the relative abundance of these two species remains difficult to quantify. The primary peaks (*m,m',s,s',t'*) appear equally in Pr₂O₃ and PrO₂, hence the assignment of peaks to a certain oxidation state becomes unlikely. Moreover, less attention has been paid for investigating Pr 3d XPS spectra than for Ce 3d. Nevertheless, it is worth noting that as the praseodymium content decreases the intensity of peak *f* weakens (the overall atomic fraction declines from 3 to about 1 percent according to the estimation from deconvoluted peaks, summarized in **Table 5**), inferring a decrease in Pr⁴⁺ content. The dominance of Ce⁴⁺ and Pr³⁺ in ceria lattice might eventually explain the expansion of lattice parameter, *a*₀, predicted previously with XRD analysis, since the ionic radius of Pr³⁺ is higher than that of Ce⁴⁺.

3.2. Reducibility of the samples

The reducibility of the samples was investigated through CO- and soot-TPR, in which samples were exposed to reductants under the increasing temperature in the absence of flowing oxygen. CO was selected as one of the reductants due to its nature as an intermediate of soot to CO₂ conversion. During the catalyst reduction, soot and CO react with both surface and bulk oxygen according to the following reaction mechanism:



CO-TPR analysis gives insight into CO conversion to CO₂ by the oxygen of the catalyst occurring in the reaction (2). This analysis presents several ideas about the typical reduction profile, e.g., reduction peaks and temperature shift, the OSC of the catalysts and the role of surface area in the reaction. To complete the understand-

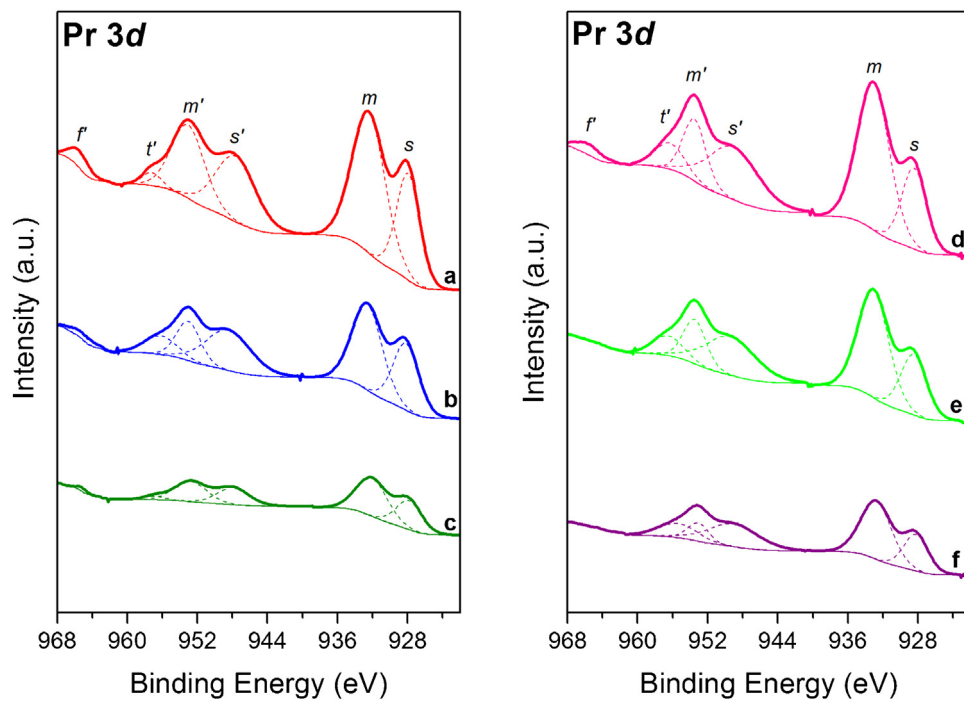


Fig. 5. XPS spectra of the (a) Ce50Pr50, (b) Ce75Pr25, (c) Ce90Pr10, (d) Ce50Pr50-SCS, (e) Ce75Pr25-SCS and (f) Ce90Pr10-SCS samples in the Pr 3d core level region.

Table 5
Results of curve-fittings on Pr 3d binding energies of catalysts.

Pr 3d _{5/2}		<i>m</i> (Pr ³⁺ /Pr ⁴⁺)		<i>s</i> (Pr ³⁺ /Pr ⁴⁺)	
Sample		(% atom)	BE (eV)	(% atom)	BE (eV)
Ce50Pr50		36.4	932.4	19.5	927.9
Ce75Pr25		32.6	932.6	22.1	928.2
Ce90Pr10		36.1	932.1	23.1	927.8
Ce50Pr50-SCS		39.5	933.1	16.9	928.4
Ce75Pr25-SCS		38.8	933.1	18.7	928.5
Ce90Pr10-SCS		37.4	932.8	19.0	928.2

Pr 3d _{3/2}		<i>m'</i> (Pr ³⁺ /Pr ⁴⁺)		<i>s'</i> (Pr ³⁺ /Pr ⁴⁺)		<i>t'</i> (Pr ³⁺ /Pr ⁴⁺)		<i>f</i> (Pr ⁴⁺)	
Sample		(% atom)	BE (eV)	(% atom)	BE (eV)	(% atom)	BE (eV)	(% atom)	BE (eV)
Ce50Pr50		18.8	953.1	20.6	947.6	1.93	957.2	2.71	965.5
Ce75Pr25		12.0	953.0	23.3	948.5	7.84	956.1	2.17	965.1
Ce90Pr10		20.4	952.8	17.0	947.9	2.28	956.9	1.12	965.2
Ce50Pr50-SCS		12.0	953.5	22.7	949.1	6.51	956.3	2.44	965.6
Ce75Pr25-SCS		12.0	953.5	23.3	949.4	7.22	956.5	–	–
Ce90Pr10-SCS		8.06	953.1	23.9	949.1	11.7	955.4	–	–

ing of the entire mechanism, including the reaction (1), the present work also resorts to soot-TPR. This method of characterizing catalyst reducibility, particularly dedicated to soot oxidation, helps understand the overall oxygen content of the catalyst, the reaction selectivity towards CO/CO₂ and lastly the importance of catalysts' intrinsic activity.

In the classical H₂-TPR tests, CeO₂ with high surface area is typically reduced in two consecutive steps: (i) surface CeO₂ reduction, in which initial removal of surface capping oxygen (α -species) at lower temperatures (300–500 °C) occurs, and (ii) bulk CeO₂ reduction, in which subsequent removal of lattice oxygen (β -species) at higher temperatures (700–1000 °C) occurs [20,40]. The latter involves transferring the lattice oxygen to the surface before reduction starts, thus higher temperature needs to be applied [41]. Nevertheless, low-temperature reduction for CeO₂ with low sur-

face area is often negligible and the main peak due to bulk reduction generally occurs at above 700 °C [20,30]. Similarly, CO-TPR analysis may give valuable information about the reducibility of ceria-based catalysts and their activity for oxidation processes [42–44].

Fig. 6 shows CO₂ concentration profiles for all catalysts. In general, CO₂ signal intensities are high for samples with high praseodymium contents, most probably due to the high amount of chemisorbed oxygens (O α). Fig. 6a shows the curves of CO₂ concentration at the outlet reactor, representing the product of CO reaction with oxygen of the catalysts. The low-temperature reduction peaks appear in ceria-praseodymia samples and the intensity is the highest for the highest praseodymium content. Praseodymium promotes the reduction of Ce⁴⁺ species, according to the XPS results (*vide supra*), and weakens the Ce-O bonds, thus favoring the formation of CO₂. Reduction peak is nearly negligible in pure ceria

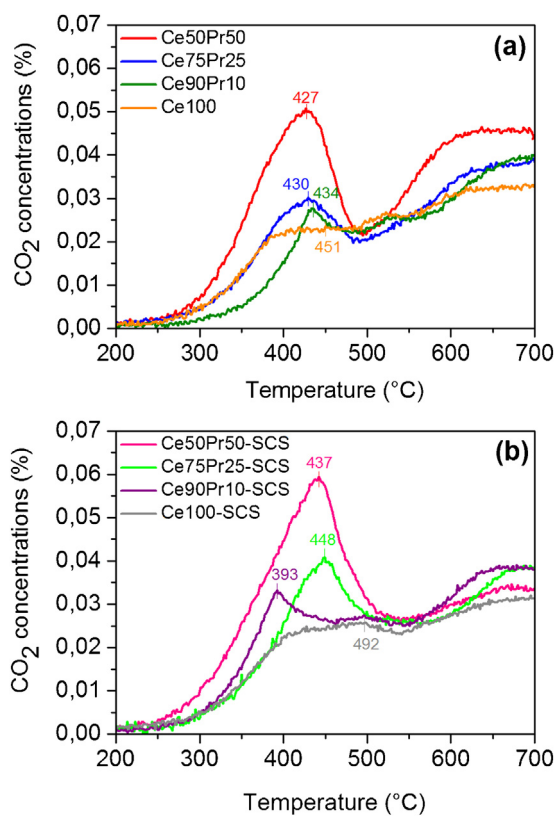


Fig. 6. CO_2 production as a function of temperature over the nanostructured (a) and SCS (b) ceria-based catalysts derived from CO-TPR analysis.

nanocubes (orange curve) due to the low surface area ceria and less amount of Ce^{3+} ions on the surface. Reduction peak shifts are clearly observed in ceria-praseodymia catalysts. The TPR peaks for all nanostructured samples appear within the temperature range of 420–440 °C. As the praseodymium content increases, the reduction peaks shifts at lower temperature, thus indicating an easier surface reducibility. This means that the insertion of Pr^{4+} ions (more reducible than Ce^{4+}) into the ceria framework promotes the catalyst reduction during the oxidation process.

The incorporation of praseodymium also increases the mobility of lattice oxygen within these nanostructured catalysts, since easier reduction of surface cerium cations in these catalysts induces more rapid bulk oxygen migration to the surface [6]. The Ce50Pr50 sample, which has the highest praseodymium content, eventually becomes the most reducible catalyst. The same reduction profiles are also observed in SCS-based catalysts. Low-temperature reduction peaks for the samples fall in the temperature range of 390–450 °C. The reduction peak at 492 °C is also noticeable in Ce100-SCS, despite having rather a broad size. This is due to the fact that the sample possesses higher surface area ($S_{\text{BET}} = 43 \text{ m}^2 \text{ g}^{-1}$) than nanostructured ceria (Ce100, $S_{\text{BET}} = 6 \text{ m}^2 \text{ g}^{-1}$). The effect of praseodymium on ceria is still evident in SCS-based materials (see Fig. 6b); ceria-praseodymia gives better reducibility than pure ceria, as the shift of peaks to low temperature range is noticeable.

The OSC was evaluated through peak deconvolution of CO_2 concentration profiles at temperatures below 500 °C. The basis of OSC calculation is the reaction of CO oxidation with lattice oxygen ($\text{CO} + \text{O}-\text{cat} \rightarrow \text{CO}_2$). The OSC reflects the amount of oxygen captured from the catalyst during the reaction, and the values are summarized on Table 6.

The data show that surface oxygen species exist more abundantly in the samples with higher praseodymium content. For both sets of catalysts, a direct relationship appears between the OSC and

Table 6

Oxygen storage capacity (OSC) derived from CO-TPR analysis (referred to CO_2 peak deconvolution at temperatures below 500 °C).

Catalysts	OSC (mmol g ⁻¹ cat)
Ce50Pr50	1.50
Ce75Pr25	1.01
Ce90Pr10	0.69
Ce100	0.43
Ce50Pr50-SCS	1.84
Ce75Pr25-SCS	1.37
Ce90Pr10-SCS	0.44
Ce100-SCS	0.35

the amount of $\text{O}\alpha$ species, derived by XPS analysis (Table 3): the higher the $\text{O}\alpha$ (at.%) the higher the OSC value. This oxygen is the major feature in soot oxidation since it helps initiate the reaction. The amount of oxygen is slightly higher in the samples synthesized through SCS and this is due to the fact that the surface areas are, in general, higher than those of nanostructured samples. This suggests the beneficial role of high surface area in improving the CO conversion to CO_2 at low temperatures, although the Pr-content has a key effect on the OSC for both sets of the prepared materials. However, the CO_2 concentrations for all samples appear to be similar above 500 °C. This means that at high temperatures the reaction seems to become surface-insensitive.

Fig. 7 summarizes the results of soot-TPR analysis. In general, soot reacts with the oxygen of the catalysts in two steps: (i) catalyst reduction at low temperatures (300–500 °C) that generates predominantly CO_2 and (ii) high-temperature reduction (>500 °C) in which CO concentration rises. These temperature ranges are somewhat similar to those in the previous analysis with CO-TPR, in which the first reduction peak appears between 300 °C and 500 °C followed by subsequent oxidation at above 500 °C. Fig. 7a and c exhibits the profiles of CO_2 concentrations of nanostructured and SCS-based catalysts, respectively. CO_2 was dominantly produced at lower temperature as seen on Fig. 7a. The reduction of the catalysts by soot at low temperatures, as expected, follows the same trend of reducibility in CO-TPR: Ce50Pr50 > Ce75Pr25 > Ce90Pr10 > Ce100. The similar trend is also observed in SCS-based samples and this further confirms the beneficial effect of praseodymium. On the other hand, the CO_2 productions over nanostructured catalysts were more intense than those over SCS-based catalysts, likely due to their higher surface reactivity for soot oxidation (=higher intrinsic activity). Since the soot-TPR profiles are rather complex and depend on non-linear interactions among different factors (i.e., OSC, soot-catalyst interaction, intrinsic reactivities, etc.) the differences in terms of CO_2 production are greater for samples with higher Pr-content. At high temperatures (>500 °C), CO_2 intensity weakens as CO concomitantly emerges, as observed in Fig. 7b and d for nanostructured and SCS-based samples, respectively. The whole analysis with soot-TPR finally discerns the roles of the two reactions in the mechanism aforementioned (*vide supra*). At low temperature, carbon soot (C) is largely converted to CO_2 , indicating a quick conversion of the intermediate (CO) to CO_2 in reaction (2). The catalysts still possess abundant surface oxygen species continuously available to undergo complete combustion of soot, as previously known in CO-TPR, therefore the formation of CO as the intermediate is inhibited. As the temperature increases until 500 °C, the oxygen species at the surface are fully released and the source of the oxygen for the reaction switches to the ones in the bulk/lattice. The liberation of this oxygen occurs so slowly since it requires extremely high energy. Therefore the oxygen supply becomes limited and only Reaction (1) can be executed.

For comparison purpose, Table 7 summarizes the amount of soot reacted during the analyses. The amount was obtained through the integral area under the CO_2 curves, starting from 150 °C to

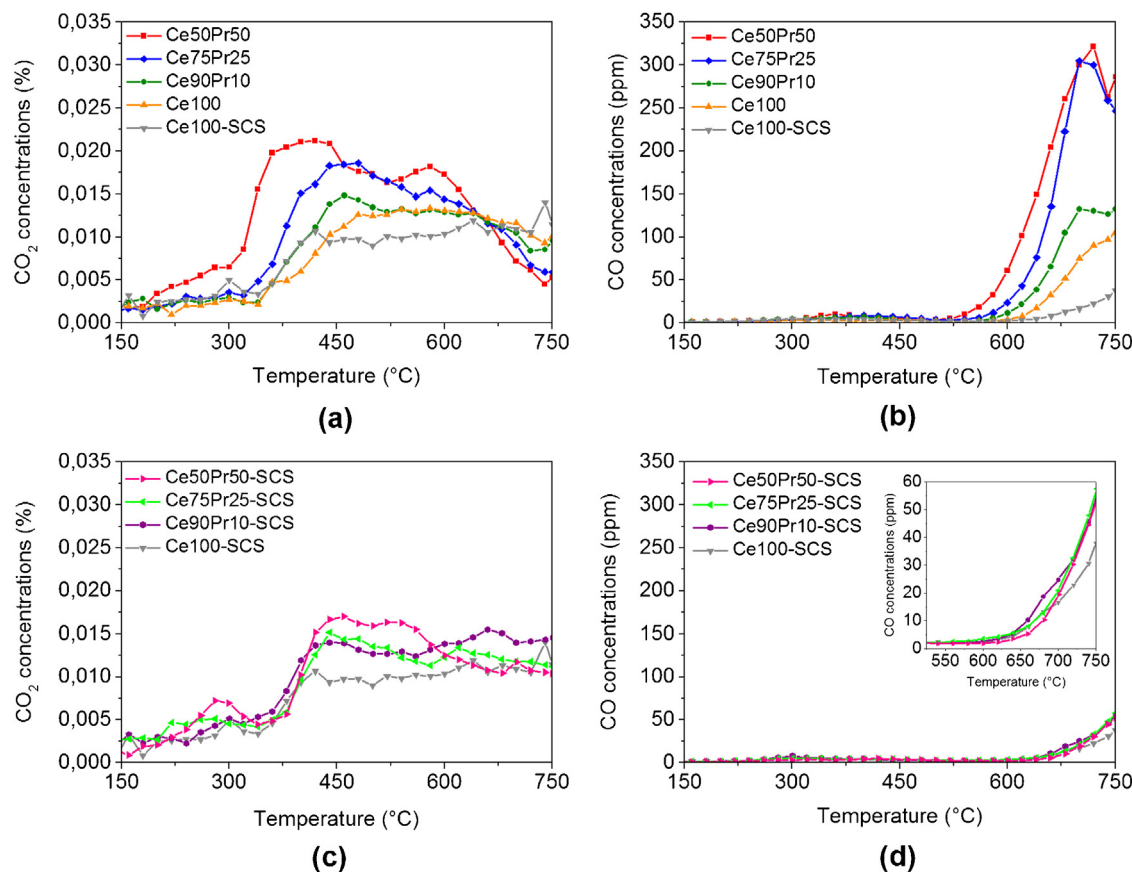


Fig. 7. Soot-TPR profiles of all prepared samples: CO₂ and CO concentrations as a function of temperature over the nanostructured (a and b) and SCS-based (c and d) catalysts.

Table 7

The amount of reacted soot derived from Soot-TPR analysis with the prepared catalysts.

Catalysts	Milligrams of soot burnt
Ce50Pr50	0.50
Ce75Pr25	0.32
Ce90Pr10	0.23
Ce100	0.19
Ce50Pr50-SCS	0.29
Ce75Pr25-SCS	0.28
Ce90Pr10-SCS	0.28
Ce100-SCS	0.21

500 °C. This range of temperature was selected in order to exclude low-temperature CO₂ desorption below 150 °C, which marks the catalyst impurities, and high-temperature CO production above 500 °C, in which different phenomena starts to occur. The ability to initiate soot combustion is the highest for both nanostructured and SCS-based catalysts with 50% praseodymium content.

3.3. Catalytic activity tests

A classical TPO analysis was used to carry out catalytic tests for soot combustion. These tests aimed at investigating the effect of morphology as well as praseodymium on the catalytic activity. Fig. 8 shows the soot conversion to CO_x as a function of temperature over nanostructured ceria-based catalysts, pure ceria-SCS (Ce100-SCS) as the initial reference and Printex-U (with the absence of catalyst) in “tight” (Fig. 8a) and “loose” contact (Fig. 8d), respectively. All catalysts performed positively in the reaction; they were able to lower the light-off temperatures compared to that for Printex-U. Soot conversions during the tests with “tight” contact appears

Table 8

Soot oxidation activity results of the prepared ceria-based catalysts under “loose” and “tight” contact conditions.

Catalyst	Contact	T10% (°C)	T50% (°C)	T90% (°C)
Ce50Pr50	Tight	360	408	441
	Loose	441	527	609
Ce75Pr25	Tight	360	412	444
	Loose	460	537	601
Ce90Pr10	Tight	384	430	458
	Loose	477	555	607
Ce100	Tight	384	435	465
	Loose	464	561	613
Ce50Pr50-SCS	Tight	395	472	532
	Loose	478	579	623
Ce75Pr25-SCS	Tight	383	460	557
	Loose	440	571	617
Ce90Pr10-SCS	Tight	362	435	505
	Loose	464	569	615
Ce100-SCS	Tight	374	440	496
	Loose	417	569	617
Printex-U	–	496	584	624

to be greatly improved compared to those of “loose” contact tests. This is due to the fact that much stronger soot-catalyst interaction and more effective mass transport phenomena occur in “tight” contact. The catalytic activity order for ceria-praseodymia catalysts conforms the reducibility trend obtained from both CO- and soot-TPR (*vide supra*). Having the lowest temperatures at which 50% of soot was reacted (408 °C and 527 °C in “tight” and “loose” contact, respectively), Ce50Pr50 becomes the most active catalyst for soot combustion among other catalysts with lower praseodymium content (values in Table 8). This finally corroborates the fact that mixing ceria with praseodymia at their equimolar composition gives the best reducibility, oxygen storage capacity and catalytic activity.

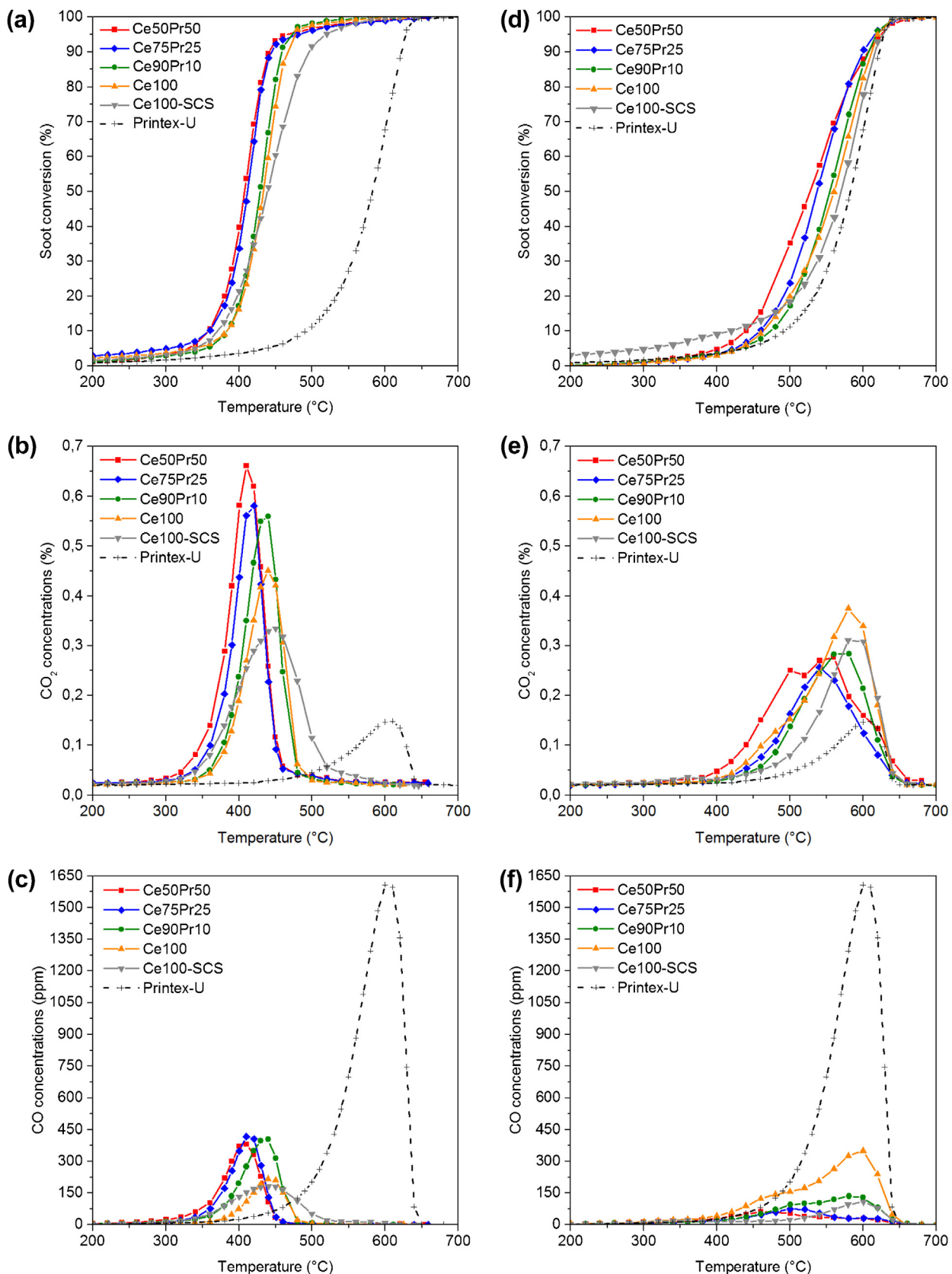


Fig. 8. Soot conversion (a and d), CO₂ concentrations (b and e) and CO concentrations (c and f) over nanostructured ceria-based catalysts under “tight” (first column) and “loose” (second column) contacts.

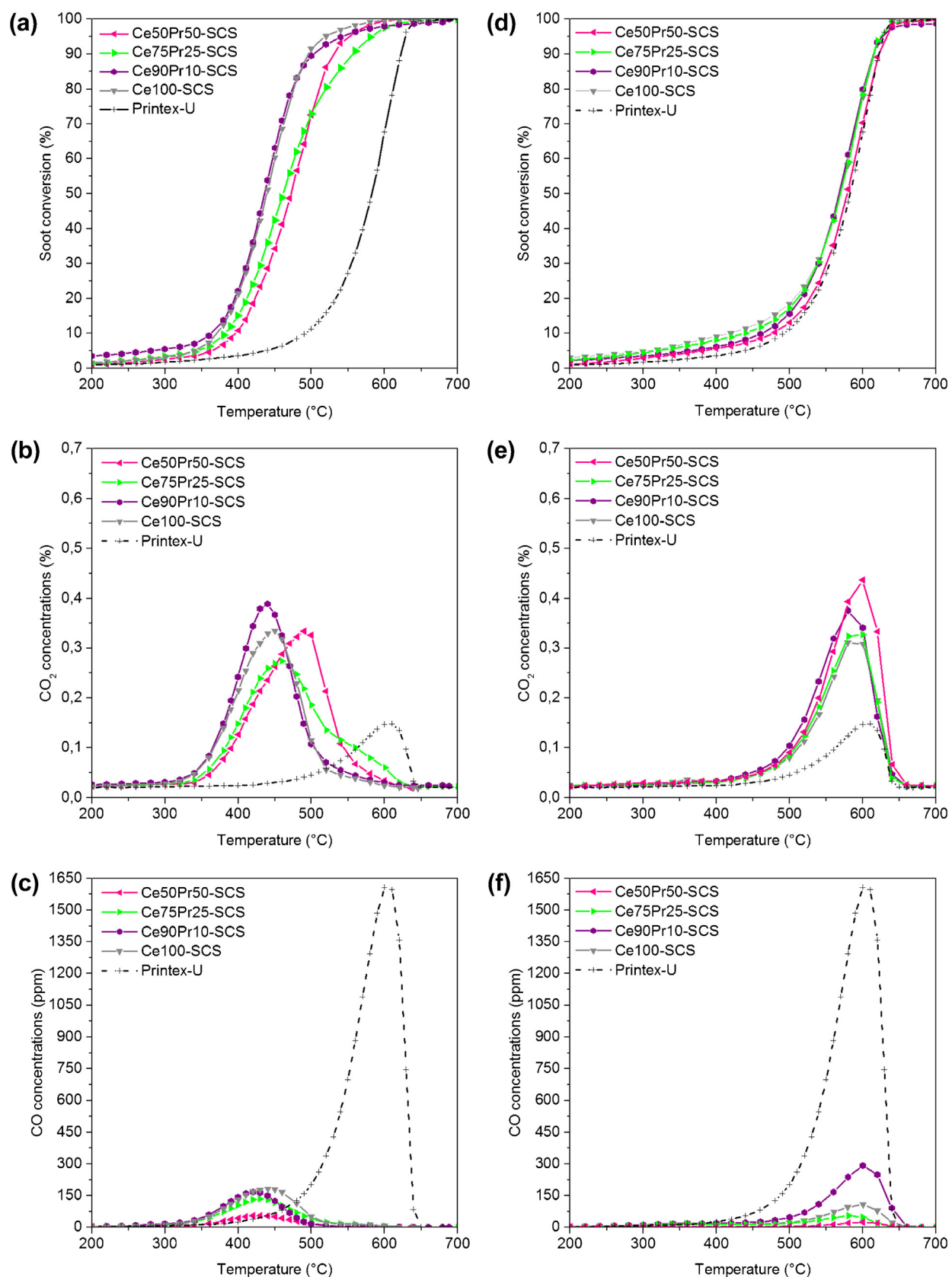


Fig. 9. Soot conversion (a and d), CO₂ concentrations (b and e) and CO concentrations (c and f) over ceria-based catalysts synthesized through SCS under "tight" (first column) and "loose" (second column) contacts.

The replacement of cerium cations with $\text{Pr}^{3+}/\text{Pr}^{4+}$ cations in ceria-praseodymia framework creates a lattice defect that enhances the number of redox sites (Ce^{3+} and Pr^{3+}) on the surface, thus generating more oxygen vacancies. These vacancies and redox sites formed during the catalytic reaction play a key role in the promoter/catalyst properties of ceria once oxygen ions are transferred from catalysts to soot.

Nanostructured ceria-based catalysts (curves with colors in Fig. 8) appear to give better soot combustion activity than pure ceria synthesized through SCS (gray curve), despite the smaller surface areas. This means that the morphology becomes another key parameter that contributes to soot catalytic activity. In general, both solution combustion and hydrothermal synthesis result in nanoscale particles; the former gives even smaller particle dimension and higher surface area than the latter. The high surface area in pure ceria-SCS sample (Ce100-SCS) explains higher activity below 400 °C, compared to pure ceria nanocubes (Ce100). However, particles obtained from SCS take form in a spongy structure that possess predominantly high index facet (111) which is the main characteristic of polycrystalline ceria [21,45]. Hydrothermal synthesis, on the contrary, allows tailoring the shape of particles constituted with well-defined planes that give more riveting reactive surfaces. Nanostructured ceria-based catalysts, as previously observed through FE-SEM, are present as nanocubes and nanorods, comprising abundant low-index surfaces with (110) and (100) orientations that are known to have high surface energies with the order following (110) < (100). At these surfaces, the respective coordination numbers (CNs) of Ce and O atoms (6 for Ce and 3 for O at (110) surface and 6 for Ce and 2 for O at (100) surface) are lower than the corresponding CNs in the bulk phase (8 for Ce and 4 for O) [23]. Hence, the surface stability is low, creating high reactivity towards soot combustion reaction. However, the catalytic activities of nanostructured ceria-praseodymia appear to vary a little albeit the clear activity order. This suggests the effect of changes in morphology due to the increasing content of praseodymium. Crystal orientation favors more nanorods than nanocubes when the praseodymium content is higher, creating more ample (110) facets that are less active than (100) facet. Nevertheless, the surface reactivity in nanostructured ceria-praseodymia catalysts remains unclear since two factors, morphology and praseodymium, are present in the materials and both play important roles.

Different effects of praseodymium, however, were observed in all SCS-based catalysts. The addition of praseodymium seems to worsen the activity of the catalyst towards soot oxidation, as observed through the conversion profiles on Fig. 9a and d, except for Ce90Pr10-SCS. Through the results of the tests with “tight” contact (Fig. 9a), it is clearly observed that the first two samples (Ce100-SCS and Ce90Pr10-SCS) have similar catalytic activities, which are higher than the activities of Ce75Pr25-SCS and Ce50Pr50-SCS. This peculiar behavior might be attributed to the surface area of the catalysts. As previously mentioned in Section 3.1, surface area decreases with the increasing amount of praseodymium in the samples. The highest activities were encountered in catalysts with low praseodymium content as well as high surface area (33 and 43 $\text{m}^2 \text{g}^{-1}$ for Ce90Pr10-SCS and Ce100-SCS respectively). It seems that in the case of SCS-based catalysts, the surface area overshadows the positive effect of praseodymium. This suggests an inevitable dependency of ceria-praseodymia catalysts on the morphology.

The profiles of CO_2 and CO concentrations as functions of temperature over nanostructured ceria-based catalysts, pure ceria-SCS and Printex-U as the comparative material are shown on Fig. 8b and c under “tight” contact and on Fig. 8e and f under “loose” contacts. The presence of catalysts, in general, renders high reaction selectivity to CO_2 and lowers the emission peaks in the 350–500 °C

temperature range. In catalytic tests with “tight contact”, which fairly eliminates the diffusive phenomena, the CO_x curves are rather sharp and narrow for nanostructured ceria-praseodymia catalysts, whilst those for SCS-based catalysts catalyst (Fig. 9b and c under “tight” contact and Fig. 9e and f under “loose” contact) are rather broad and low in intensity. This suggests the occurrence of mass transport limitations (e.g., Knudsen diffusion) within the porous framework of SCS catalysts [20]. This also reflects in the soot conversion curves, in which Ce100-SCS conversion curve possesses lower slope.

4. Conclusion

Ce50Pr50 catalyst (where 50 indicates the atomic percentage of cerium as well as of praseodymium) with well-defined nanostructures (nanorods and nanocubes) has attained the best catalytic performances, thanks to its high lattice oxygen mobility and its high reducibility. The replacement of cerium cations with $\text{Pr}^{3+}/\text{Pr}^{4+}$ gives advantages in the increasing number of redox sites on the surface, thus enabling more oxygen vacancies. Despite having low surface area, nanostructured ceria-praseodymia catalysts were able to mediate soot combustion reaction more actively than SCS-based ceria-praseodymia catalysts with larger surface areas. The beneficial effect of well-defined nanostructures was eventually known, involving low-index surfaces with coordinative unsaturated atoms that are reactive towards soot combustion reaction. Such positive effect was not observed in the catalysts synthesized through solution combustion synthesis (SCS), since in this case the specific surface area becomes more important and contributes more than praseodymium to the overall catalytic activity. This finally concludes that ceria-praseodymia solid solution functions better along with well-defined nanostructures. Such synergistic combination has a great potential for future development.

Acknowledgments

The Ministero dell'Università e della Ricerca (MIUR) (grant number: RBFR12LS6M 001) is acknowledged for sponsoring this research activity (FIRB – Futuro in Ricerca 2012). This work was also co-funded through a SINCHEM Grant. SINCHEM is a Joint Doctorate programme selected under the Erasmus Mundus Action 1 Programme (FPA 2013-0037). Authors thank Camilla Galletti for XRD measurements, Mauro Raimondo for FE-SEM measurements and Salvatore Guastella for XPS analysis.

References

- [1] P. Eastwood, *Critical Topics in Exhaust Gas After Treatment*, Research Studies Press Ltd., Baldock, England, 2000, pp. 400.
- [2] A. Trovarelli, C. de Leitenburg, M. Boaro, G. Dolcetti, *Catal. Today* 50 (1999) 353–367.
- [3] A. Trovarelli, *Catal. Rev. Sci. Eng.* 38 (1996) 439–520.
- [4] R. Di Monte, J. Kašpar, *Top. Catal.* 28 (2004) 47–58.
- [5] A. Trovarelli, P. Fornasiero, *Catalysis by Ceria and Related Materials*, 2nd ed., Imperial College Press, London, 2013, pp. 565–621.
- [6] A. Bueno-López, *Appl. Catal. B* 146 (2014) 1–11.
- [7] A. Gupta, U.V. Waghmare, M.S. Hegde, *Chem. Mater.* 22 (2010) 5184–5198.
- [8] K. Krishna, A. Bueno-López, M. Makkee, J.A. Moulijn, *Appl. Catal. B* 75 (2007) 210–220.
- [9] G. Thrimurthulu, K.N. Rao, D. Devaiah, B.M. Reddy, *Res. Chem. Intermed.* 38 (2012) 1847–1855.
- [10] N. Guillén-Hurtado, A. García-García, A. Bueno-López, *Appl. Catal. B* 174 (2015) 60–66.
- [11] S. Bensaid, G.A. Blengini, D. Fino, N. Russo, *Chem. Eng. Commun.* 201 (2014) 1327–1339.
- [12] D. Fino, V. Specchia, *Chem. Eng. Sci.* 59 (2004) 4825–4831.
- [13] E. Cauda, D. Fino, G. Saracco, V. Specchia, *Top. Catal.* 45 (2007) 125–129.
- [14] S. Bensaid, N. Russo, D. Fino, *Catal. Today* 216 (2013) 57–63.
- [15] P.A. Kumar, M.D. Tanwar, S. Bensaid, N. Russo, D. Fino, *Chem. Eng. J.* 207–208 (2012) 258–266.

- [16] J.M. Thomas, R. Raja, *Top. Catal.* 53 (2010) 848–858.
- [17] K. An, G.A. Somorjai, *Catal. Lett.* 145 (2015) 233–248.
- [18] T.X.T. Sayle, S.C. Parker, C.R.A. Catlow, *Surf. Sci.* 316 (1994) 329–336.
- [19] A. Vantomme, Z.-Y. Yuan, G. Du, B.-L. Su, *Langmuir* 21 (2005) 1132–1135.
- [20] M. Piumetti, S. Bensaid, N. Russo, D. Fino, *Appl. Catal. B* 165 (2015) 742–751.
- [21] E. Aneggi, D. Wiater, C. De Leitenburg, J. Llorca, A. Trovarelli, *ACS Catal.* 4 (2014) 172–181.
- [22] H.-X. Mai, L.-D. Sun, Y.-W. Zhang, R. Si, W. Feng, H.-P. Zhang, H.-C. Liu, C.-H. Yan, *J. Phys. Chem. B* 109 (2005) 24380–24385.
- [23] J. Paier, C. Penschke, J. Sauer, *Chem. Rev.* 113 (2013) 3949–3985.
- [24] S.C. Laha, R. Ryoo, *Chem. Commun.* (17) (2003) 2138–2139.
- [25] R.D. Shannon, *Acta Cryst. A* 32 (1976) 751–767.
- [26] K. Krishna, A. Bueno-López, M. Makkee, J.A. Moulijn, *Top. Catal.* 75 42–43 (2007) 221–228.
- [27] P.X. Huang, F. Wu, B.L. Zhu, G.R. Li, Y.L. Wang, X.P. Gao, H.Y. Zhu, T.Y. Yan, W.P. Huang, S.M. Zhang, D.Y. Song, *J. Phys. Chem. B* 110 (2006) 1614–1620.
- [28] A. Dodd, *J. Colloid Interface Sci.* 392 (2013) 137–140.
- [29] J.-G. Kang, B.-K. Min, Y. Sohn, *J. Alloys Comp.* 619 (2015) 165–171.
- [30] P. Ji, J. Zhang, F. Chen, M. Anpo, *J. Phys. Chem. C* 112 (2008) 17809–17813.
- [31] H. Chen, A. Sayari, A. Adnot, F. Larachi, *Appl. Catal. B: Environ.* 32 (2001) 195–204.
- [32] A.K. Sinha, K. Suzuki, *J. Phys. Chem. B* 109 (2005) 1708–1714.
- [33] M. Piumetti, S. Bensaid, N. Russo, D. Fino, *Appl. Catal. B Environ.* 180 (2016) 271–282.
- [34] B.M. Reddy, A. Khan, Y. Yamada, T. Kobayashi, S. Loridant, J.-C. Volta, *J. Phys. Chem. B* 107 (2003) 5162–5167.
- [35] T. Brezesinski, C. Erpen, K. Iimura, B. Smarsly, *Chem. Mater.* 17 (2005) 1683–1690.
- [36] J. Gurgul, M.T. Rinke, I. Schellenberg, R. Pöttgen, *Solid State Sci.* 17 (2013) 122–127.
- [37] S. Lütkehoff, M. Neumann, *Phys. Rev. B* 52 (1995) 13808–13811.
- [38] H. Ogaswara, A. Kotani, R. Potze, G.A. Sawatzky, B.T. Thole, *Phys. Rev. B* 44 (1991) 5465–5469.
- [39] A. Bianconi, A. Kotani, K. Okada, R. Giorgi, A. Gargano, A. Marcelli, T. Miyahara, *Phys. Rev. B* 38 (1988) 3433–3437.
- [40] F. Giordano, A. Trovarelli, C. de Leitenburg, M. Giona, *J. Catal.* 193 (2000) 273–282.
- [41] G. Ranga Rao, B.G. Mishra, *Bull. Catal. Soc. Ind.* 2 (2003) 122–134.
- [42] Z. Wu, M. Li, S.H. Overbury, *J. Catal.* 285 (2012) 61–73.
- [43] M. Boaro, M. Vicario, C. de Leitenburg, G. Dolcetti, A. Trovarelli, *Catal. Today* 77 (4) (2003) 407–417.
- [44] T. Caputo, L. Lisi, R. Pirone, G. Russo, *Appl. Catal. A* 348 (2008) 42–53.
- [45] K.B. Zhou, X. Wang, X.M. Sun, Q. Peng, Y.D. Li, *J. Catal.* 229 (2005) 206–212.